Constrained sintering and cracking of air plasma sprayed thermal barrier coatings: Experimental observation and modelling

Xun Zhang[1*], Alan C.F. Cocks[1], Yoshifumi Okajima[2], Kazuma Takeno[2], Taiji Torigoe[2]

[1]Department of Engineering Science, University of Oxford, Parks Road, Oxford OX1 3PJ, UK

[2]Mitsubishi Heavy Industries, Ltd. 1-1 Shinhama, 2-chome, Arai-cho, Takasago, Hyogo, 676-8686, Japan

Abstract:

The development of vertical cracks in air plasma sprayed (APS) thermal barrier coatings (TBCs) during thermal cycling and constrained sintering under a temperature gradient is investigated. Microstructural analysis shows that the development of the vertical cracks is associated with multiple processes, including sintering during the hold period and cleavage during cooldown. Inspired by the experimental observations, an image-based sintering model is used to simulate the development of vertical cracks as the coating sinters while constrained by a substrate. The computational results show that microstructural imperfections can develop into vertical cracks, which then propagate towards the interface. A simple analytical model is presented for the threshold level of in-plane stress for the onset of propagation of a vertical crack during constrained sintering. By combining the results of these different modelling approaches, the cross-coupling of the material and geometric parameters, and how this determines the sintering response (microstructure evolution) and vertical crack formation is evaluated. In addition, the growth of vertical cracks by a cleavage mechanism during cooldown is examined and the coupling between sintering, cleavage crack growth and TBC lifetime is explored.

Key words: Sintering; Lifetime; Modelling; Crack propagation; High temperature

1. Introduction

Yttria-stabilised zirconia (YSZ) thermal barrier coatings (TBCs) made by air plasma spray (APS) are increasingly used in gas turbine components to provide thermal and environmental protection [1]. However, the relatively larger scatter in lifetime is preventing the full potential of these types of coatings from being achieved [2, 3].

*Corresponding author: Tel. +44 7784 679728
E-mail address: xun.zhang@eng.ox.ac.uk; xun.zhang@manchester.ac.uk
Present address: Henry Royce Institute for Advanced Materials, Department of Materials, University of Manchester, Manchester M13 9PL, UK

The lifetime of APS TBCs strongly depends on the coatings' microstructure and its evolution under service conditions [3]. During deposition, curvy YSZ splats form as the molten YSZ particles flow and undergo rapid solidification upon reaching the substrate [4]. Microstructural defects, including inter-splat cracks and equiaxed pores also form during deposition. These defects play an important role in determining the thermal conductivity and strain tolerance of the coating [1].

In service, where the temperature at the coating surface can be as high as 1300°C and a thermal gradient as large as 600°C/mm is seen across the coating thickness [1], progressive healing (sintering) of the inter-splat cracks occurs [5]. Moreover, sintering of the coating is constrained by the metal substrate. This leads to the build-up of an in-plane stress which promotes vertical cracking [6, 7]. Once nucleated, the vertical cracks can relax the constraint on sintering and accelerate sintering locally. This further drives the growth of the vertical cracks, which propagate towards the interface and link up with horizontal defects, which in turn propagate parallel to the plane of the coating, leading to delamination and failure of the TBC, as observed in a laser thermal gradient test [8]. Understanding the formation of vertical cracks and how they couple with sintering is important to fully understand and prevent TBC failure under realistic service conditions.

Zhu et al. studied wedge-shaped vertical cracks in APS TBCs and associated them with the creep strain and the resultant tensile stress generated upon cooling and associated their growth with a cleavage mechanism [9]. However, the relatively large opening of the vertical cracks, especially at the coating surface, suggests that they are related to sintering at high temperature. Clifton Bumgardner et al. conducted in-situ thermal cycling tests and found that vertical crack initiation was driven by the in-plane tensile stress in the coating when heating from a stress-free state [10]. However, their tests were conducted under isothermal conditions. For practical applications, the coating surface experiences the highest temperature, and therefore experiences the largest expansion during heating up. A compressive stress is expected in the coating near the surface which is unlikely to generate vertical cracks. More recently, Chen et al. examined the same region of an APS TBC at different stages of

sintering and demonstrated that sintering can lead to micro-crack nucleation from microstructural imperfections [11]. Kumar et al. have developed models to simulate crack formation from microstructural imperfections in the sintering process for an EB-PVD TBC [12, 13]. In their macroscopic constitutive model, the YSZ columns make contacts at asperities and the imperfection is treated as a volume of material where the initial asperity contact radius is smaller than that within the rest of the coating. They found that imperfections can develop into cracks when the coating's in-plane modulus exceeds a critical value. These studies indicate the importance of sintering on the development of vertical cracks. However, the detailed processes that result in the development and growth of vertical cracks during constrained sintering of an APS TBC remain unclear.

In this study, we describe a series of constrained sintering tests under a temperature gradient which provide insights into the formation and development of vertical cracks as the coating sinters. We then employ the computational sintering model developed in [5] to evaluate how macroscopic cracks can develop from microscopic defects in the structure during constrained sintering. The computational model makes direct use of micrographs of the coating and employs models of sintering (and desintering) across contacting (microcracked) surfaces using an adaptation of the sintering asperity model developed in [14]. The main features of the computational models are summarised in Appendix A. In these image-based computational models, we focused on the early stages of the formation and propagation of vertical cracks driven by the sintering of the adjacent material. The aim is to identify the conditions that favour the development of vertical cracks during constrained sintering. The understanding gained from these computational models underpin the development of a simple analytical model for the growth of a vertical crack in a sintering body, which identifies the conditions under which a small defect can develop into a macroscopic crack.

Stresses generated within the coating during thermal cycling are much larger than those induced during the high-temperature hold period as a result of the constrained sintering. These high stresses can promote the propagation of the vertical cracks by a cleavage mechanism [15]. We also evaluate this

mechanism here and demonstrate how a crack can propagate through a combination of sintering at the hold temperature and cleavage during cooldown, leading to failure of the coating after a number of thermal cycles.

2. Cracks formed after constrained sintering in a laser thermal gradient test

Button samples with a diameter of 30mm for thermal cycling and sintering were produced by APS. The as-sprayed TBC is 1mm thick. A CO_2 laser was used to heat the sample surface to the target temperature at a controlled rate. During the test, the temperature at the TBC surface was monitored by an infrared thermometer while the temperature at the TBC/bondcoat interface was monitored by extrapolating the temperatures measured inside the substrate at two different distances from the interface using embedded thermocouples. The samples were then subjected to different surface temperatures for different periods. The temperature gradient across the TBC during the hold period was kept at 600°C/mm for all tests. The samples were then cooled to ambient conditions, while the temperatures were monitored to determine the history of the surface and bondcoat temperature as the sample cooled.

Specimens for microstructure characterisation were cut form the centre of the test buttons. The cross-sectional micrographs are compared in Figure 1 for three different hold conditions. Micrographs of the as-deposited material are given in [5]. The samples contain pores and microcracks of the order of the size of the YSZ splats. Figure 1 (a)-(c) show that for all the three conditions, multiple large vertical cracks have developed. The total length of the cracks is comparable for the three cases and is about 500-600µm. The magnified SEM micrographs of the cracks in Figure 1 (d)-(f) show that all the vertical cracks have a wedge-shaped opening profile near the surface and a thin yet uniform opening towards the crack tips. Moreover, the longer the dwell time and the higher the hold temperature, the wider the opening of the cracks.

If it is assumed that these vertical cracks have developed during cooldown from the hold temperatures, the opening of the crack at the coating surface due to thermal expansion mismatch as the coating cools down to ambient (i.e. 25°C) can be calculated as:

$$\delta_{\text{surf}} = \frac{4\times 1.12^2}{\pi}\left(\left[(T_s^s - 25)\alpha_{TBC} - (T_I^s - 25)\alpha_{SUBS}\right]\pi a - (T_s^s - T_I^s)\alpha_{TBC}a^2\right) \quad (1)$$

where α_{TBC} and α_{SUBS} are the thermal expansion coefficients of the TBC and the substrate respectively. We take α_{TBC} equal to 1.0x10^{-5}/K and α_{SUBS} equal to 1.5x10^{-5}/K [15]. T_s^s and T_I^s are the temperatures at the coating surface and interface during the hold period of the sintering test. a is the length of the vertical crack. According to Eqn. (1), the crack opening at the coating surface is estimated to be about 2-3μm which is one order of magnitude smaller than those shown in Figure 1 (d)-(f). In fact, the observation that a higher surface temperature and a longer sintering time leads to a larger crack opening at the coating surface suggests that these cracks have developed at least partially and opened at the sintering temperatures. The small yet uniform opening profiles near the roots suggest that these segments could have been generated upon cooldown from the sintering temperatures by a cleavage mechanism driven by the thermal stress.

In addition to the large, wedge-shaped vertical cracks, finer vertical cracks and horizontal cracks are observed at the coating surface and near the interface after constrained sintering, see Figure 2. The finer vertical cracks in Figure 2 (a) are observed between the large wedge-shaped vertical cracks shown in Figure 1 (a)-(c). Notice in Figure 2 (a) that the nearly horizontal inter-splat cracks have largely sintered, especially near the vertical crack. Several residual inter-splat crack segments can be seen below the tip of the vertical crack. These observations suggest that the fine vertical cracks in Figure 2 (a) have nucleated during sintering and relaxed the constraint on sintering locally, leading to faster sintering near them. Some of these nucleated cracks can propagate further, relax the constraint on sintering to a larger depth and develop into the large and wedge-shaped cracks shown in Figure 1. Meanwhile, propagation of these vertical cracks will relax the in-plane stress that has built up during

sintering. As a result, other vertical cracks (such as that shown in Figure 2 (a)) will remain stationary or even sinter. Nevertheless, the vertical crack in Figure 2 (a) can be regarded as an early-stage state of the large wedge-shaped cracks shown in Figure 1.

In the subsequent sections, we first simulate the formation of vertical cracks like those shown in Figure 2 (a) from microstructural imperfections, and their propagation during constrained sintering (Section 3). This is followed by a simple analytical model to relate the geometrical parameters with the onset of vertical crack propagation during sintering (Section 4). Moreover, the effect of thermal stress on the evolution of vertical cracks during transient heating and cooling cycles experienced in laser thermal gradient tests is demonstrated (Section 5). Finally, the conditions for unstable coating delamination once a vertical crack reaches the interface are probed (Section 6).

3. Model results for constrained sintering

The image-based sintering model developed in [5] is employed to simulate the constrained sintering response of the TBC. The model takes the micrograph of an as-deposited TBC as input and yields the microstructure evolution as a result of sintering. We start by examining the constrained sintering of a coating containing a fully developed vertical crack. We demonstrate that the influence of sintering of a coating having the microstructure of an as-deposited APS TBC on the vertical crack can be reproduced by the sintering of an array of nearly vertical cracks. We then consider the constrained sintering response of coatings containing microstructural imperfections and explore the conditions under which these can develop into cracks as represented by Figure 2 (a). Unless otherwise stated, the geometrical and material constants used in this study are the same as listed in Table 1 in [5].

3.1 Constrained sintering response of coatings containing a developed crack

Constrained sintering of a coating containing a fully-developed vertical crack as represented by the cross-sectional SEM micrograph in Figure 3(a) is investigated. This micrograph has been taken from the root of one of the wedge-shaped cracks about 600µm below the coating surface. During the sintering test, the temperature in this region was relatively low (~1040°C assuming a linear

temperature distribution through the coating). Considering the relatively short hold period in the sintering tests, the micrography can still represent the microstructure of the as-deposited TBC. Therefore, the sintering model is implemented on an FE mesh mapped onto this micrograph, as shown in Figure 3 (b).

During the simulation, the horizontal displacement of the vertical edges is constrained. A multiple point constraint is imposed on the bottom surface so that it remains straight during the sintering simulation, while the top surface is allowed to displace freely. Cocks and Fleck have shown that for an APS TBC under constrained sintering, the in-plane stress decays via Coble creep from their initial values to a level on the order of the sintering stress over a timescale of $\tau_1 \equiv \eta / E$ [4]. For the typical YSZ properties at 1300°C, τ_1 is on the order of tens of seconds [2]. Therefore, for simplicity, the thermal stresses generated during the transient heating to the sintering temperature is neglected and the coating is assumed to be stress-free initially in the constrained sintering simulations.

The vertical crack is characterised by a much larger initial opening so that the crack surfaces are not in contact. The simulation results in Figure 3 (c) and (d) show that when the TBC is constrained, sintering of the curvy inter-splat cracks can lead to the opening of the existing vertical crack. This is related to the curvy nature of the inter-splat cracks, since constrained sintering of an array of perfectly horizontal cracks will only produce a vertical sintering strain, which does not promote opening of the vertical crack. As a result of the traction free boundary condition on the vertical crack surfaces, the constraint on sintering near the vertical crack is partially relaxed, thus promoting a higher local sintering rate and opening of the crack. For example, Crack ①, which lies next to the vertical crack, has sintered faster than Crack ②, that lies far away despite having a similar opening profile and orientation.

3.2 Constrained sintering response of coatings containing imperfections and vertical cracks

We now analyse the formation of a vertical crack from a microstructural imperfection during constrained sintering, as represented in Figure 2 (a), and its subsequent propagation. Since significant sintering has occurred within the region shown in Figure 2 (a), an array of nearly vertical microcracks, whose surfaces are bridged by asperities, are introduced to represent the sintering of the coating. The resultant FE mesh is shown in Figure 4 (a) and the bridged microcracks are indicated by the arrows. The initial contact geometry (expressed in terms of the asperity contact radius) is uniform for the surfaces indicated by the black arrows. These are referred to as precursor cracks. Three cases representing the early stage of vertical crack nucleation and propagation are examined. In the first case, we focus on the nucleation of a vertical crack from a microstructural imperfection. The microstructural imperfection, as highlighted by the red arrow in Figure 4 (a), is referred to as a microcrack bridged by asperities with a smaller initial contact radius. The influence of sintering in the adjacent material on the imperfection is reproduced by the sintering of the precursor cracks. This simplification is based on the model results in the previous sub-section that the sintering of the nearly horizontal, yet curvy inter-splat cracks has promoted the opening of the vertical crack, which can be reproduced by the sintering of the precursor cracks.

We take the initial asperity contact radius as $b = 0.87\mu m$ at the precursor cracks and $b = 0.77\mu m$ at the imperfection. These correspond to an initial average opening of 190nm to 204nm for the precursor cracks and imperfection. This is in line with mercury intrusion porosimetry (MIP) results for crack width in an as-sprayed APS TBC [16]. The sintering responses for different choices for the viscosity of the YSZ splats (via different splat thickness $2h$) are assessed. The temporal evolution of the average asperity contact radius at the imperfection and the neighbouring precursor crack (see Figure 4 (b)) is compared in Figure 5 (a). For h=2µm, the YSZ splats are creep compliant and the imperfection and the precursor crack have sintered in a similar manner. This is because the sintering strain can be readily accommodated by Coble creep of the YSZ splats. As a result, the interaction between the precursor

cracks and the imperfection as they sinter remains limited. For h=10 μm, the imperfection desinters and turns into a crack (i.e. the asperity contact radius reduces to zero). The steps in the curve for the imperfection in Figure 5(a) (i.e. red dash line) is a result of desintering and cracking progressing gradually from the surface. Once nucleated, the crack opens and relaxes the constraint on sintering of the cracks nearby, allowing them to sinter faster. This effect is demonstrated by the relatively faster growth of the asperity contact radius at the precursor crack as the imperfection disinters (the red solid line) than the case where no imperfection has been included in the simulation (the red dash-dot line).

Once the imperfection develops into a crack, the in-plane tensile stress is intensified at its tip, especially when the YSZ splat is viscous, which can promote desintering at the tip, allowing the crack to propagate further. This, coupled with opening of the crack due to creep of the splats and sintering of adjacent crack-like features, leads to the development of the wedge-shaped crack shown in Figure 1. In order to demonstrate this mechanism, the FE mesh in Figure 4 (a) has been modified such that the imperfection is replaced with a crack whose surfaces are not in contact and a precursor region of finite asperity contacts ahead of the crack tip. This is shown in Figure 4 (c). Within the precursor region, the initial asperity contact radius gradually increases over a length of ~10μm. The resultant average initial asperity contact radius within the precursor region is close to that for the precursor cracks (i.e. $\overline{b} = 0.87\,\mu m$ for the precursor region).

The temporal evolution of the average contact radius for the crack tip precursor region is compared with that of the neighbouring precursor crack in Figure 5 (b). For h=2μm, sintering is observed at both locations. Notice that the sintering rate is lower at the precursor region than at the neighbouring precursor crack. Comparison of the stresses in Figure 6 confirms that the lower sintering rate is due to the larger tensile traction across the crack tip precursor region. Still, the precursor region sinters and brings the initial contact-free crack surfaces into contact, leading to the full sintering of the crack. For h=10μm, the precursor region has desintered progressively as indicated by the stepwise decrease of the average asperity contact radius. According to Figure 6, both the in-plane stress and the traction

in the precursor region are larger for h=10μm. The larger normal traction in the precursor region has led to the progressive desintering. Once desintered, the traction across the cracked surfaces drops to zero. Consequently, the average traction in the precursor region (see the red dash line in Figure 6) has dropped stepwise.

In the above simulations we have idealised the geometry in terms of a series of nearly vertical cracks. In practice the coating contains many nearly horizontal inter-splat cracks. These will influence the behaviour of the vertical cracks, either changing their path, or arresting their growth. We explore this by considering the situation shown in Figure 4 (d) in which the vertical crack has connected with a nearly horizontal inter-splat crack. We place a precursor region of finite asperity contacts running almost vertically near to the opposite end of the horizontal defect. The evolution of the average asperity contact radius for this precursor region and the neighbouring precursor crack is compared in Figure 5 (c) for h=2μm and 10μm. Similar to the previous example, the precursor region has sintered for h=2μm and desintered progressively for h=10μm.

This idealised result can be generalised to the situation where a vertical crack meets a number of intersecting inter-splat cracks as it propagates. Instead of cutting through the splat directly, it follows the inter-splat crack and propagates along the weakest path whether it be a vertical intra-splat crack, or more generally, a gap between two splats which may be partially bridged by asperities. This scenario is confirmed by the cross-sectional SEM micrograph taken from an as-sintered sample as shown in Figure 7. The actual crack path depends on the detailed crack network while the simulation results represent a simplified version of this. Nonetheless, the simplified situation considered here provides insights into how and why a crack is deflected as it propagates through the thickness of the coating and helps explain the observations of crack deflection, such as that shown in Figure 7.

4. Conditions for vertical crack propagation during sintering

The simulations in the previous section demonstrate how imperfections in an APS TBC can develop into vertical cracks. As the coating sinters, a tensile in-plane stress is generated such that the creep

deformation associated with the YSZ splats matches the deformation as a result of the sintering of the inter-splat cracks. The magnitude of the in-plane stress depends on the local sintering potential for the asperities, the characteristic viscosity associated with asperity sintering and the viscosity of the YSZ splats. This in-plane tensile stress can promote vertical crack nucleation from microstructural imperfections. Once nucleated, the vertical crack can intensify the in-plane stress at the tip, which may drive the crack further into the coating. On the other hand, the nucleated cracks can also re-sinter as the simulations demonstrate. The exact response depends on (1) the magnitude of the in-plane stress (the driving force) and (2) the threshold value of the in-plane stress for a vertical crack with a sintering zone ahead of its tip to propagate (the resistance).

As a first step to estimate the in-plane stress level, we employ the brick model developed by Cocks et al. [14], from which an analytical expression for the in-plane stress during constrained sintering can be obtained. We further simplify the problem by assuming that asperities at the top and bottom of the splats are aligned with the coating's out-of-plane direction. The in-plane stress now reads:

$$\sigma = \left(1 + \frac{3\pi R n_a^s b^4}{8\chi h^3}\right)^{-1} \sigma_s = \left(1+\xi\right)^{-1} \sigma_s \tag{2}$$

where R is the average splat radius; $\chi = d/2h$ is the aspect ratio of the columnar grains within the YSZ splats and σ_s represents the in-plane sintering potential associated with the asperities on the vertical surfaces of the YSZ splats. σ_s depends on the surface and interfacial energies, the contact conditions and the density of the asperities on the vertical surfaces of the YSZ splats n_a^s, see [14] for the details.

The quantity

$$\xi = \frac{3\pi R n_a^s b^4}{8\chi h^3} \tag{3}$$

is a purely geometric parameter that describes the relative magnitude of the viscosity for asperity sintering to that for Coble creep of the YSZ splats.

When the splat viscosity is much higher than the asperity viscosity (e.g. a large h), the in-plane stress approaches σ_s . On the contrary, when the splat is compliant, the in-plane stress is relaxed by Coble creep of the YSZ splats, leading to a smaller in-plane stress. This is in accordance with the computational results presented above, where in each of the cases analysed, the vertical crack has propagated for h=10μm and has sintered for h=2μm. Note that Eqn. (2) assumes that all the inter-splat cracks are readily bridged by asperities [14] while in practice the inter-splat cracks become bridged by asperities progressively from local regions such as crack tips and local pinning points [5]. The opening of the un-bridged crack segments gives rise to additional compliance of the coating. Additionally, the sintering potential evolves with the number of sintering asperities (i.e. asperities that are in contact, but not fully sintered). Both can change the level of the in-plane stress. Nevertheless, Eqn. (2) captures the major physical processes during constrained sintering and provides a first order assessment of the significance of different material and geometric parameters on the in-plane stress level.

At the sintering temperature, the APS TBC is assumed to undergo linear, transversely isotropic creep with the x_3 - direction normal to the plane of isotropy. The strain rate is given by:

$$\dot{\boldsymbol{\varepsilon}} = \mathbf{H}\boldsymbol{\sigma} \tag{4}$$

where $\mathbf{H}$ is the creep matrix for the coating material. $\mathbf{H}$ has contributions from the opening of un-bridged inter-splat cracks, Coble creep of the YSZ splats and the diffusional growth of the asperity contact area [14]. The components of $\mathbf{H}$ depend strongly on the sintering response, especially the inter-splat crack evolution of the APS TBC. For an as-deposited coating, the inter-splat cracks are well separated leading to large values for the components of $\mathbf{H}$. As the coating sinters, more inter-splat cracks close and heal by asperity sintering across their surfaces. Moreover, the average asperity contact radius increases, leading to an increased asperity viscosity. The viscosity of the YSZ splat also increases due to grain growth. As a result, components of $\mathbf{H}$ decrease as sintering proceeds. The minimum values for the components of $\mathbf{H}$ are expected when the coating fully sinters and $\mathbf{H}$ now

becomes equal to the Coble creep matrix $\mathbf{\Pi}$ for the YSZ splats given in Eqn. (A7). In this extreme, the components of $\mathbf{H}$ scale with $3\mathcal{D}_g / \left(\chi h^3\right)$, where $\mathcal{D}_g$ is the effective boundary diffusivity [5].

For plane problems with the x_3- direction normal to the coating surface, the creep matrix $\mathbf{H}$ is reduced to a dependency upon six independent constants:

$$\mathrm{H}'_{ij} = \begin{cases} \mathrm{H}_{ij} & \text{Plane stress} \\ \mathrm{H}_{ij} - \dfrac{\mathrm{H}_{i2}\mathrm{H}_{j2}}{\mathrm{H}_{22}} & \text{Plane strain} \end{cases} \qquad (i, j = 1,3,5) \tag{5}$$

The threshold level of in-plane stress for a vertical crack at the coating surface with an initial length a (much smaller than the coating's thickness) to propagate at the sintering temperature is determined in Supplemental Materials S1 using the path independence of the C* integral. It can be estimated as:

$$\sigma_{th} = T_s \left(1 + 2.5\pi a \lambda \mathrm{H}'_{11} \mathrm{A}\right)^{-1/2} \tag{6}$$

where T_s is given by Eqn. (A4) and represents the traction at the sintering zone ahead of the crack. In an APS TBC sample, it depends on the surface and interfacial energies, the contact conditions and the density of the asperities on the surfaces at the sintering zone; λ is given by Eqn. (A3) and is the viscosity arising from asperity sintering and depends on the effective boundary diffusivity, the asperity contact radius and contacting asperity density in the sintering zone [14]. The parameter

$$\mathrm{A} = \sqrt{\frac{\mathrm{H}'_{33}}{2\mathrm{H}'_{11}}} \left[\sqrt{\frac{\mathrm{H}'_{33}}{\mathrm{H}'_{11}}} + \frac{\mathrm{H}'_{13} + 2\mathrm{H}'_{55}}{\mathrm{H}'_{11}} \right]^{1/2} \tag{7}$$

quantifies the degree of anisotropy and is equal to unity for an isotropic material.

The full derivation of Eqn. (6) and its validation using FE simulations are provided in Supplemental Materials S1. According to Eqn. (6), two characteristic length scales can be identified: a geometric

length scale (a) and a material length scale ($1/\left(\lambda \mathrm{H}_{11}^{'}\mathrm{A}\right)$). The threshold stress is related to the sintering traction T_s in the sintering zone via the ratio of these two length scales. A large initial crack length a and a small value of $1/\left(\lambda \mathrm{H}_{11}^{'}\mathrm{A}\right)$ leads to a lower threshold stress for crack propagation at the sintering temperature.

Specifically for a brick model, the creep matrix of the coating material reads [14]:

$$\mathbf{H} = \mathbf{\Pi} + \mathbf{\Lambda}^{-1} \tag{8}$$

where $\mathbf{\Lambda}$ is the viscosity tensor arising from asperity sintering, whose components scale with asperity viscosity which scales with $b^4/\mathcal{D}_g$, asperity density n_a^s and the YSZ splat radius R, see Appendix B of [14]. A dimensionless parameter I for the onset of vertical crack propagation can be obtained by combining Eqn. (6) and (2):

$$I \equiv \frac{\sigma}{\sigma_{th}} = \frac{\sigma_s\left(1+2.5\pi a\lambda \mathrm{H}_{11}^{'}\mathrm{A}\right)^{1/2}}{T_s\left(1+\xi\right)} = G\frac{\sigma_s}{T_s} \tag{9}$$

Crack propagation occurs when $I>1$. Adopting the following geometric values: $R=50\mu m$, $d=0.3\mu m$, $b=0.87\mu m$, $s=5.5\mu m$ and $a=25\mu m$, the degree of anisotropy A, the relative viscosities associated with splat creep and asperity sintering ξ and the geometrical factor G in Eqn. (9) can be determined and are plotted in Figure 8 as functions of the normalised splat thickness. The crack length a is measured directly from Figure 2 (a); the value for b is taken to be the same as in the computational model and all other material and geometric parameters are consistent with our previous free sintering simulations [5]. According to Figure 8 (a), the value of A decreases slightly from 4.15 to 3.15 as the value of h changes from 2 μm to 10 μm. The magnitude of ξ decreases from about 10 to 0.1 with increasing splat thickness. More importantly, increasing the splat thickness will lead to a larger value for G and therefore promotes crack propagation according to Eqn. (9).

Recall from the simulation that a larger h also promotes the nucleation of a crack from an imperfection. Consequently, a larger initial crack length a is expected for a larger h, which again favours crack propagation. Note, as the crack length a increases, I increases, so once the condition for crack propagation is met, it will continue to grow through the thickness of the coating.

5. Coupled effect of sintering and thermal cycling

Cracks can propagate by desintering along planes of incomplete sintering through the thickness of the coating, but when there is a large thermal gradient (i.e. 600°C/mm in the sintering test), the rates of the kinetic processes associated with asperity sintering and Coble creep decrease rapidly with distance from the surface of the coating. Thus, we might expect the above mechanism of crack growth to occur only near the surface region. This is at variance with the experimental observations of cracks in the as-sintered samples, where the large, wedge-shaped vertical cracks have propagated through more than half of the coating thickness (see Figure 1). On the other hand, the opening at the roots of these cracks is much smaller and more uniform than near the surface, which suggests a transition to a cleavage mechanism as the crack grows. The possibility of propagation by cleavage from a sintering crack during cooldown is now analysed.

We assume that the coating is stress free at the end of a high-temperature hold period and the temperature varies linearly from the coating surface to the interface (in practice there will be a small in-plane stress generated by the constraint on the sintering process imposed by the substrate as described above – but this is much smaller than any stresses generated due to thermal mismatch and can thus be ignored in the current context). During cooldown, we assume that the cooling rate is high enough to suppress any stress relaxation, so that the in-plane stress within the coating at a distance y from the coating surface can be estimated as:

$$\sigma(y) = \frac{E(y)}{1-\nu}\left[\alpha_{TBC}\left(T^s(y) - T(y)\right) - \alpha_{SUBS}\left(T_I^s - T_I\right)\right] \tag{10}$$

We ignore the sintering-induced variation in the elastic modulus within the TBC for now (i.e. $E(y)$ is uniform and evolves with sintering time). Upon cooldown, the thermal stress in the TBC is tensile at the surface and switches to compressive at the interface. Consequently, the thermal stress will produce a pure Mode I stress intensity factor (SIF) at the tip of the sintering crack if it lies in the tensile region and may potentially drive it to propagate further. A simple elastic FE model is developed to estimate the level of the SIF at the tip of a pre-existing vertical crack. A repeating unit with one vertical crack in the middle as shown in Figure 9 is modelled.

The width of the region considered is taken as the average spacing between two vertical cracks in Figure 1 (~1.2 mm). Periodic boundary conditions are applied to the left and right edges of the region of the body shown in Figure 9. The coating is 1mm thick and is bonded to a substrate 6mm thick. The coating and the substrate cool down to ambient simultaneously with an initial temperature that varies linearly from 1400°C at the coating surface to 800°C at the interface. The stress intensity factor after cooldown is determined for different initial crack lengths a .

In the sintering test and real service condition, faster cooling is expected at the coating surface as the engine shuts down (i.e. a thermal shock condition [15, 17, 18]). The effect of this on the stress intensity factor is examined by introducing an intermediate state. During cooldown, the surface and interface temperatures first drop to 320°C at the intermediate state. Afterwards the coating and substrate cool down to room temperature simultaneously. In the subsequent sintering cycle, the surface and interface temperatures reach those at the hold period simultaneously. This temperature hysteresis is demonstrated in Figure 10. For simplicity, we assume a piece-wise linear variation of temperature between these states.

The FE results for the variation of the SIF with the initial crack length at the intermediate state and room temperature is shown in Figure 11. At both states, the normalised SIF increases with the initial crack length a when a is small. As a becomes larger, the SIF drops as the crack approaches the compressive zone. This gives rise to a plateau in the SIF. The onset of crack propagation depends on

the relative magnitude of the SIF associated with the initial crack length a and the fracture toughness of the coating. When the SIF exceeds the fracture toughness, the vertical crack will propagate. As it propagates, the SIF at its tip may increase firstly (depending on the initial crack length) and eventually drops gradually. The crack will arrest as the SIF drops below the fracture toughness again. In addition, a higher SIF that spans a larger thickness through the coating is observed at the intermediate state. Therefore, vertical crack propagation is promoted by thermal shock. This is consistent with the experimental observation that fast cooling leads to reduced TBC lifetime during thermal cycling in burner rig tests [18]. It is worth noting that the SIF scales with the coating's Young's modulus. Sintering can promote vertical crack growth during cooldown by increasing the coating's Young's modulus and encouraging a larger initial length a for the vertical cracks.

Once developed, the vertical cracks will relax the constraint on sintering in the subsequent sintering cycles, allowing the coating surface to sintering faster and leading to increased thermal conductivity locally. In practice, the hot gas can also ingress to the interior of the coating through the vertical cracks. Therefore, a higher temperature to a greater depth than the linear temperature profile is expected during subsequent sintering. This will accelerate the sintering process, promote vertical crack propagation during sintering and generate tensile stresses over a larger depth as the coating cools down. This couples with the evolving modulus profiles of the coating and provides an ever-increasing driving force for the entire vertical crack growth process.

6. Vertical cracks as free edges for delamination

As the vertical cracks approach the interface, they can interact and link with intrinsic defects generated during coating deposition and/or horizontal cracks that have developed near the interface during cyclic sintering [15]. Unstable delamination occurs when the energy release rate for a linked horizontal crack exceeds the interfacial toughness, leading to coating spallation as observed in cyclic laser thermal gradient tests of 160h duration in [8]. In this section we evaluate the conditions under which the growth of a delamination crack can become unstable.

We assume that a vertical crack has fully developed and assess the driving force for growth of a connected horizontal crack. As noted earlier, the in-plane stress is relaxed by Coble creep of the YSZ splats and asperity sintering during the high temperature hold period. Prior to cooldown, the in-plane stress within the TBC is negligible. During cooldown, the in-plane stress is given by Eqn. (10). This stress distribution gives rise to energy stored in the coating that can be released to drive the growth of the delamination crack. For simplicity, we assume that the delamination crack lies within the YSZ topcoat at a small distance from the interface, which is of the order of the splat size (Figure 2 (b)) so that consideration of the Dundur's parameters α and β is not required. This problem has been analysed by Fleck et al. [15] and we follow their analysis here. Fleck et al. [15] have formulated the in-plane modulus as a linear function of the Larson-Miller parameter seen by the TBC locally when the in-plane modulus lies within 20-110GPa. Here, we set a lower bound to the modulus such that:

$$E(y) = \max\left\{\kappa\left(\ln t + 30 - \ln 2\right)T^s(y) + c,\ E_{\text{as-deposited}}\right\} \tag{11}$$

where $T^s(y)$ is the temperature at a distance y from the coating surface during sintering; κ and c are constants that can be determined by fitting experimental data. We adopt $\kappa = 5.5\ \text{MPa}$ and $c = -275\ \text{GPa}$ as determined by Fleck et al. [15]. We further assume that the as-deposited coating has a uniform in-plane modulus of ~20GPa [15, 17].

The energy release rate and mode mixity can be determined as a function of the instantaneous temperature distribution during cyclic sintering as shown in Figure 10. The results are shown in Figure 12 for different sintering conditions. The key equations to produce Figure 12 are reproduced from [15] and listed in Supplemental Materials S2. If no sintering is considered, the maximum energy release rate has remained below 60J/m^2 during cooldown and delamination is unlikely. After sintering for 10h, the average modulus increases, leading to an increased energy release rate upon cooldown. In this case, the maximum energy release rate occurs at the intermediate state and reaches about 100J/m^2. Moreover, the coating becomes stiffer closer to the surface after sintering under a temperature

gradient. Consequently, a larger stress gradient is expected during cooldown after sintering, which may potentially lead to a decreased mode mixity (larger component of mode I) as shown in Figure 12(b). This can also promote delamination. The energy release rate increases further after sintering for 100h and delamination becomes more likely.

From the previous analysis, two timescales can be identified that determine the onset of delamination: (i) the time for a vertical crack to propagate through the thickness and link up with the defects near the interface (i.e. deflect parallel to the interface) and (ii) the time for the coating to sintering to a stiffness large enough to induce an energy release rate that is higher than the coating's toughness upon cooldown. The actual TBC lifetime depends on the slower of the two processes.

7. Conclusions

Through a series of calculations and evaluation of TBC coated samples that have been subjected to different hold periods at high temperature and cooled to ambient conditions, a detailed mechanism of vertical crack nucleation and propagation in the coating is proposed.

- The intrinsic defects in an APS TBC provide the necessary precursors for the initiation of macroscopic cracks. Wedge-shaped cracks first initiate from defects at the surface during hold period in a sintering test. These cracks grow and open as a result of desintering at the tip of the crack and sintering and creep of the adjacent material.
- The nucleation and propagation of the vertical cracks at the sintering temperature is encouraged by a larger viscosity of the YSZ splats (i.e. thicker splats), a lower sintering traction in the micro-cracked sintering zone and a longer initial crack length.
- The vertical cracks developed during a hold period can further propagate during cooldown driven by the thermal stresses generated due to the mismatch in thermal expansion with the substrate. Therefore, as the temperature is cycled the crack grows through a combination of sintering induced cracking during a hold period and cleavage during cooldown.

- As a vertical crack reaches the interface, it can deflect by linking with the incipient horizontal defects and/or cracks that have developed in the coating during sintering. Once deflected, the vertical cracks serve as free edged for delamination. Sintering leads to an increased modulus and therefore an increased driving force for vertical crack growth and delamination.

Acknowledgements

This work was supported by Mitsubishi Heavy Industries (MHI), Japan. XZ is grateful for the help on the user element development from Dr. Elsiddig Elmukashfi.

Appendix A The image-based FE model

The key features of the computational model for sintering are briefly summarised. Central to this model is a contact law for the cracks that sinter progressively. The faces of the sintering cracks are rough, which is described by a regular array of asperities. The crack surfaces are assumed to be in contact only if the local opening is less than the initial height of an asperity, which is simplified as a spherical cap. Once in contact, asperity sintering driven by the surface energy and surface traction occurs and pulls the crack faces towards each other. This closes the crack and brings more asperities on the crack faces into contact. In the meantime, diffusional flow along the columnar grain boundaries leads to Coble creep of the YSZ splats, which relaxes the constraint on asperity sintering.

Consider a unit area of crack that is bridged by asperities. We assume simplified geometric profiles for the changing shape of the asperities as they sinter. The asperities are initially assumed to be spherical caps. As they sinter, their apexes are replaced by cylinders with contact radius b, while their base radius R_0 remains constant until b becomes equal to R_0. Subsequent sintering leads a simultaneous increase in the contact radius and base radius, and they are then modelled cylinders, which gradually flatten as the contact radius grows and volume of the asperities is conserved.

The centre-to-centre distance between two neighbouring asperities is s. The number of asperities per unit area follows as:

$$n_a = \frac{2\sqrt{3}}{3s^2} \tag{A1}$$

Driven by the net reduction in surface energy and the potential energy of the applied traction, matter diffuses from the contacts with an interfacial energy γ_g to the side of the asperity with a surface energy γ_s.

Using the thermodynamic variational principle described by Cocks et al [19], the crack opening rate by asperity sintering can be determined, and is related to the normal traction:

$$T_n = \lambda \dot{w}_n^s + T_s \tag{A2}$$

where λ is an effective viscosity associated with asperity sintering:

$$\lambda = \frac{n_a \pi b^4}{8\mathcal{D}_{gb}} \tag{A3}$$

and

$$T_s = \frac{n_a A(\gamma_s, \gamma_g, b)}{B(b)} \tag{A4}$$

Is a sintering potential. Here, $\mathcal{D}_g$ is the temperature-dependent effective boundary diffusivity given by:

$$\mathcal{D}_g = \frac{\delta\Omega}{kT} D_0 \exp\left(-Q / RT\right) \tag{A5}$$

A is a function of the contact geometry and the surface and interface energy while B is a function of the contact geometry only. The expressions for A and B are given in Appendix A1 of [5].

The contacting asperities at the bridged crack segments endow the crack surfaces with a finite contact stiffness such that

$$T_n = k(b, s) w_n^e \tag{A6}$$

Its value depends non-linearly on the contact radius b and the spacing between the asperities s. Following Fleck et al. [2], $k(b, s)$ is obtained by interpolating the extreme values for small b/s and b/s close to 0.5.

The YSZ splats comprising of columnar grains are assumed to follow a linear, transversely isotropic creep response. Following Cocks et al. [14], the columnar grains are idealised as ellipsoids with the long

axis aligned with the direction normal to the splat surface (local z-direction). The strain rate reads using a Voigt notation:

$$\begin{bmatrix} \dot{\varepsilon}_x \\ \dot{\varepsilon}_y \\ \dot{\varepsilon}_z \\ \dot{\gamma}_{yz} \\ \dot{\gamma}_{zx} \\ \dot{\gamma}_{xy} \end{bmatrix} = \frac{3\mathcal{D}_g}{\chi h^3} \begin{bmatrix} \frac{1+\chi^2}{\chi^2(\chi+2)} & -\frac{1}{\chi^2(\chi+2)} & -\frac{1}{\chi+2} & & & \\ -\frac{1}{\chi^2(\chi+2)} & \frac{1+\chi^2}{\chi^2(\chi+2)} & -\frac{1}{\chi+2} & & & \\ -\frac{1}{\chi+2} & -\frac{1}{\chi+2} & \frac{2}{\chi+2} & & & \\ & & & \frac{4}{\chi+1} & & \\ & & & & \frac{4}{\chi+1} & \\ & & & & & \frac{2}{\chi^2} \end{bmatrix} \begin{bmatrix} \sigma_x \\ \sigma_y \\ \sigma_z \\ \tau_{yz} \\ \tau_{zx} \\ \tau_{xy} \end{bmatrix} = \mathbf{\Pi\sigma} \tag{A7}$$

The components of $\mathbf{\Pi}$ are determined by the effective boundary diffusivity $\mathcal{D}_g$, the splat thickness h and the aspect ratio of the columnar grains $\chi = d / 2h$.

The grain size is assumed to follow a cubic growth law at the sintering temperature:

$$d^3 - d_0^3 = kt \tag{A8}$$

where the grain growth constant k is determined by fitting measurements taken from SEM micrographs presented in [20].

References

1. N. P. Padture, M. Gell, and E. H. Jordan, "Materials science - Thermal barrier coatings for gas-turbine engine applications," *Science,* 296[5566] 280-84 (2002).

2. N. A. Fleck and A. C. F. Cocks, "A multi-scale constitutive model for the sintering of an air-plasma-sprayed thermal barrier coating, and its response, under hot isostatic pressing," *J Mech Phys Solids,* 57[4] 689-705 (2009).

3. E. P. Busso, J. Lin, S. Sakurai, and M. Nakayama, "A mechanistic study of oxidation-induced degradation in a plasma-sprayed thermal barrier coating system. Part I: Model formulation," *Acta Mater,* 49[9] 1515-28 (2001).

4. A. C. F. Cocks and N. A. Fleck, "Constrained sintering of an air-plasma-sprayed thermal barrier coating," *Acta Mater,* 58[12] 4233-44 (2010).

5. X. Zhang, A. C. F. Cocks, Y. Okajima, K. Takeno, and T. Torigoe, "An image-based model for the sintering of air plasma sprayed thermal barrier coatings," *Acta Mater,* 206 116649 (2021).

6. F. Li, J. Z. Pan, and A. Cocks, "Defect Healing and Cracking in Ceramic Films During Constrained Sintering," *J Am Ceram Soc,* 95[12] 3743-49 (2012).

7. A. Jagota and C. Y. Hui, "Mechanics of Sintering Thin-Films .2. Cracking Due to Self-Stress," *Mech Mater,* 11[3] 221-34 (1991).

8. Y. S. Wu, P. F. Hsu, Y. Wang, M. H. McCay, D. E. Croy, D. Moreno, L. He, C. Wang, and H. Q. Zhang, "Laser Thermal Gradient Testing and Fracture Mechanics Study of a Thermal Barrier Coating," *J Therm Spray Techn,* 28[6] 1239-51 (2019).

9. D. M. Zhu and R. A. Miller, "Thermal conductivity and elastic modulus evolution of thermal barrier coatings under high heat flux conditions," *J Therm Spray Techn,* 9[2] 175-80 (2000).

10. C. Bumgardner, B. Croom, and X. D. Li, "High-temperature delamination mechanisms of thermal barrier coatings: In-situ digital image correlation and finite element analyses," *Acta Mater,* 128 54-63 (2017).

11. Y. Chen, C. Li, X. F. Zhao, and P. Xiao, "Measurements and understanding of the stiffness of an air plasma sprayed thermal barrier coating," *Surf Coat Tech,* 394 (2020).

12. S. Kumar and A. C. F. Cocks, "Computational modelling of constrained sintering in EB-PVD thermal barrier coatings," *Model Simul Mater Sc,* 21[6] (2013).

13. S. Kumar and A. C. F. Cocks, "Sintering and mud cracking in EB-PVD thermal barrier coatings," *J Mech Phys Solids,* 60[4] 723-49 (2012).

14. A. Cocks, N. Fleck, and S. Lampenscherf, "A brick model for asperity sintering and creep of APS TBCs," *J Mech Phys Solids,* 63 412-31 (2014).

15. N. A. Fleck, A. C. F. Cocks, and S. Lampenscherf, "Thermal shock resistance of air plasma sprayed thermal barrier coatings," *J Eur Ceram Soc,* 34[11] 2687-94 (2014).

16. S. Paul, "Assessing Coating Reliability Through Pore Architecture Evaluation," *J Therm Spray Techn,* 19[4] 779-86 (2010).

17. J. W. Hutchinson and A. G. Evans, "On the delamination of thermal barrier coatings in a thermal gradient," *Surf Coat Tech,* 149[2-3] 179-84 (2002).

18. R. Vaßen, D. E. Mack, M. Tandler, Y. J. Sohn, D. Sebold, and O. Guillon, "Unique performance of thermal barrier coatings made of yttria-stabilized zirconia at extreme temperatures (>1500°C)," *J Am Ceram Soc,* 104[1] 463-71 (2021).

19. A. C. F. Cocks, S. P. A. Gill, and J. Z. Pan, "Modeling microstructure evolution in engineering materials," *Adv Appl Mech,* 36 81-162 (1999).

20. G. R. Li, H. Xie, G. J. Yang, G. Liu, C. X. Li, and C. J. Li, "A comprehensive sintering mechanism for TBCs-Part I: An overall evolution with two-stage kinetics," *J Am Ceram Soc,* 100[5] 2176-89 (2017).

Figure captions

Figure 1 Cross-sectional micrographs of the as-sintered coatings. (a)-(c) global optical micrographs of coatings after sintering at: (a) surface temperature 1500°C, TBC/bondcoat interface temperature 900°C for 8h; (b) surface temperature 1400°C, TBC/bondcoat interface temperature 800°C for 4h and (c) surface temperature 1400°C, TBC/bondcoat interface temperature 800°C with no dwell time. The yellow arrows indicate the vertical cracks. (d)-(f) Zoomed-in SEM micrographs of the regions in the yellow rectangles in (a)-(c).

Figure 2 Cross-sectional SEM micrographs of the sample after sintering at a surface temperature of 1400°C for 4h showing (a) a fine vertical crack at the surface of the TBC between the large wedge-shaped cracks and (b) a horizontal crack near the topcoat/bondcoat interface.

Figure 3 Computational model of the sintering response of an area containing a vertical crack: (a) SEM (SE) micrograph of the area; (b) the FE mesh based on (a) and the prescribed boundary condition for the constrained sintering simulation. Two cracks with similar opening profiles and orientations are highlighted by the ellipses; (c) and (d) the predicted microstructure after sintering at 1300°C for 38h and 126 h. The vertical crack has been opened by the progressive sintering of the nearly horizontal inter-splat cracks.

Figure 4 (a) FE mesh derived from Figure 2 (a). The arrows indicate the introduced microcracks. (b-d): magnified view of the rectangular region in (a) for the three cases investigated. The yellow braces highlight the precursor regions at the crack tips.

Figure 5 Temporal evolution of the predicted average asperity contact radius at (a) the imperfection; (b) and (c) the precursor region at the crack tip together with that at the neighbouring precursor crack for a YSZ splat thickness of 2μm and 10μm respectively.

Figure 6 Evolution of the in-plane stress and surface traction averaged over the precursor region for h=2μm and 10μm respectively.

Figure 7 Cross-sectional SEM micrograph showing a sintering crack that has been deflected by the inter-splat cracks at the coating surface during constrained sintering.

Figure 8 Plots of (a) the degree of anisotropy A in Eqn. (7); (b) the logarithm of the relative viscosity ξ in Eqn. (3) and (c) the geometric factor G in Eqn. (9) with respect to the normalised splat thickness. The splat thickness has been normalised against the asperity contact radius.

Figure 9 Schematics of the repeating unit with a crack of length a in the middle. Periodic boundary conditions are applied to both sides of the area.

Figure 10 The cool down/reheat cycle from an initial hold temperature during the sintering test down to room temperature via an intermediate state upon cooling and reheating to the hold temperature.

Figure 11 Variation of the stress intensity factor normalised against the coating's in-plane modulus with the initial vertical crack length normalised against the coating thickness at the intermediate temperature (red) and room temperature (blue).

Figure 12 Contours of (a) energy release rate and (b) the mode mixity as a function of the instantaneous temperature distribution when the coating with thickness of 1mm cools down from the sintering temperature (1400°C at TBC surface and 800°C at interface) after sintering for different periods. The white lines indicate the component temperature history in one cooling-reheating cycle. The black dash lines in (b) show the instants where the SIF for a delamination crack is pure Mode I.

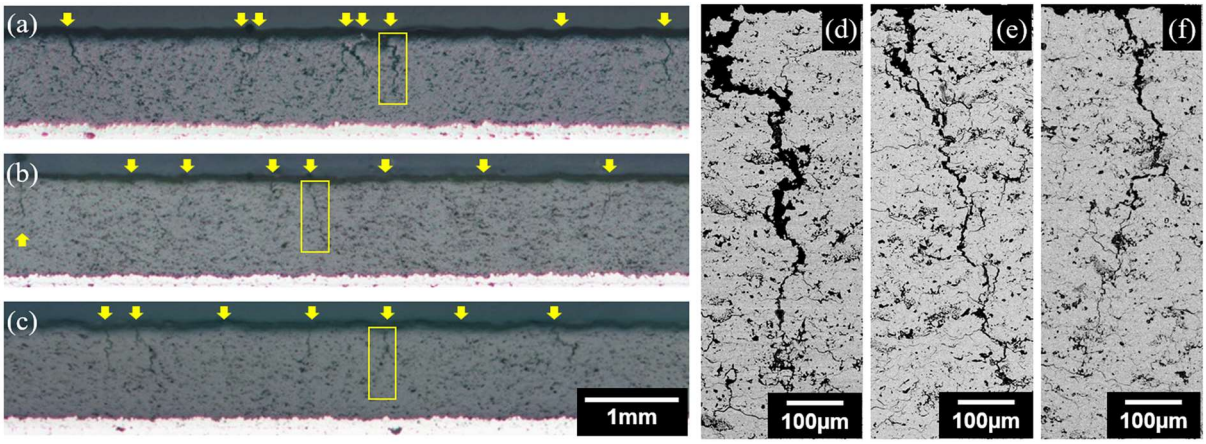

Figure 1 Cross-sectional micrographs of the as-sintered coatings. (a)-(c) global optical micrographs of coatings after sintering at: (a) surface temperature 1500°C, TBC/bondcoat interface temperature 900°C for 8h; (b) surface temperature 1400°C, TBC/bondcoat interface temperature 800°C for 4h and (c) surface temperature 1400°C, TBC/bondcoat interface temperature 800°C with no dwell time. The yellow arrows indicate the vertical cracks. (d)-(f) Zoomed-in SEM micrographs of the regions in the yellow rectangles in (a)-(c).

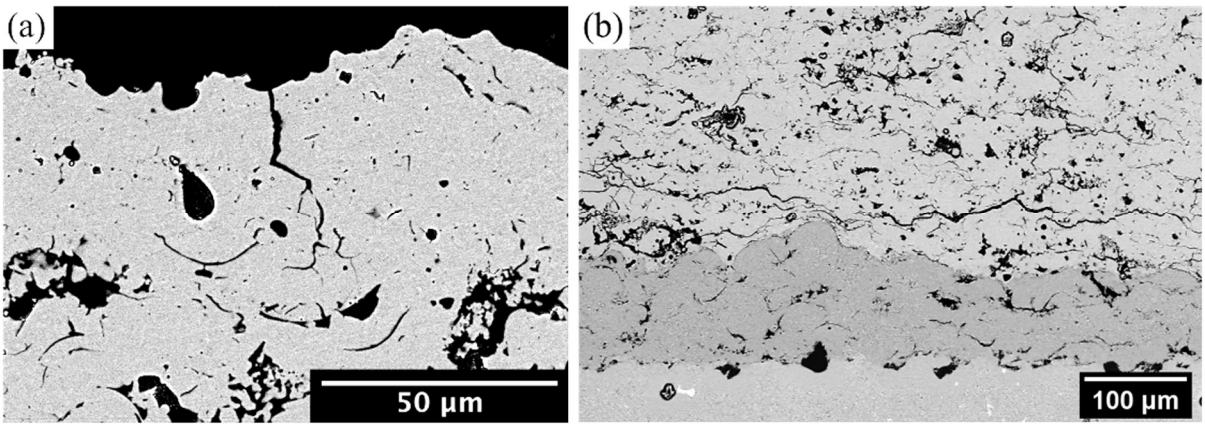

Figure 2 Cross-sectional SEM micrographs of the sample after sintering at a surface temperature of 1400°C for 4h showing (a) a fine vertical crack at the surface of the TBC between the large wedge-shaped cracks and (b) a horizontal crack near the topcoat/bondcoat interface.

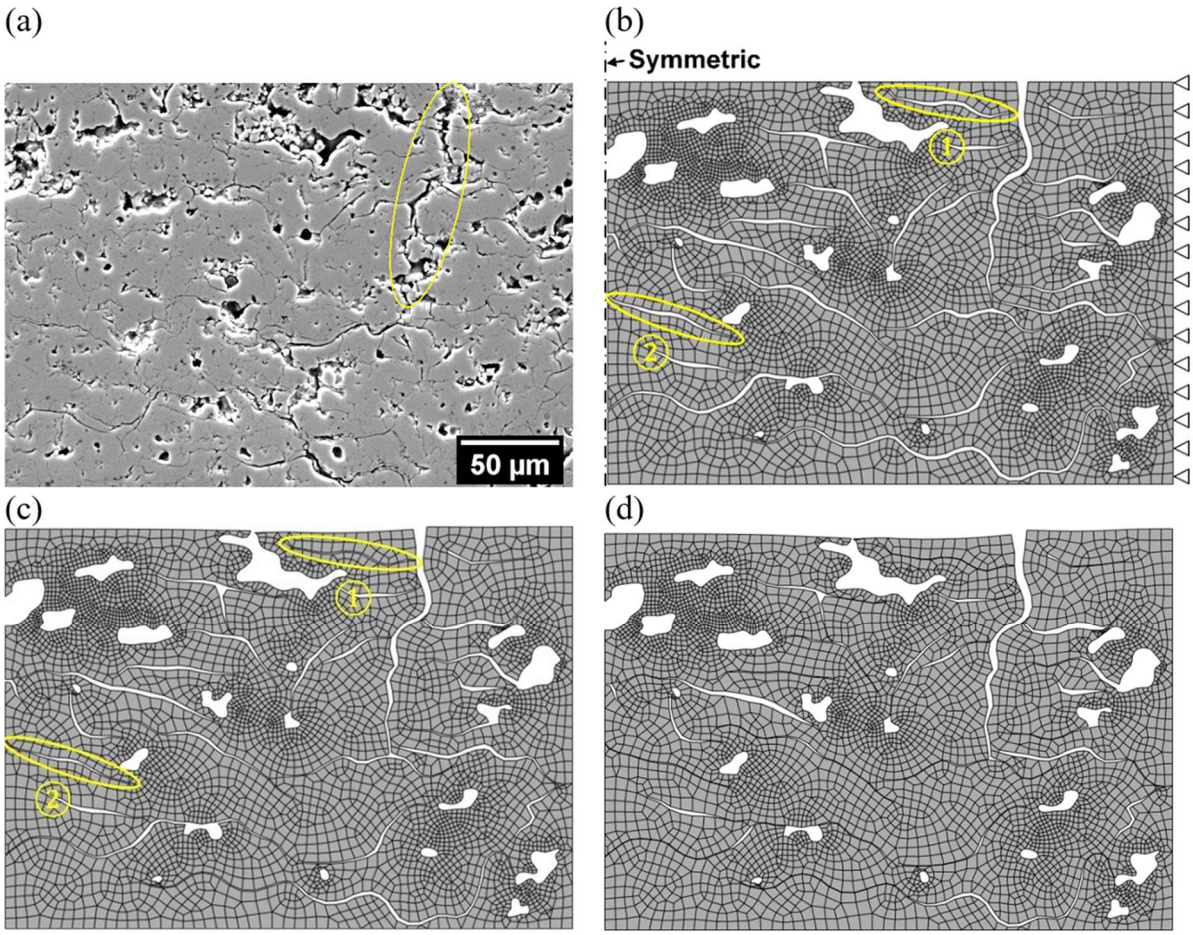

Figure 3 Computational model of the sintering response of an area containing a vertical crack: (a) SEM (SE) micrograph of the area; (b) the FE mesh based on (a) and the prescribed boundary condition for the constrained sintering simulation. Two cracks with similar opening profiles and orientations are highlighted by the ellipses; (c) and (d) the predicted microstructure after sintering at 1300°C for 38h and 126 h. The vertical crack has been opened by the progressive sintering of the nearly horizontal inter-splat cracks.

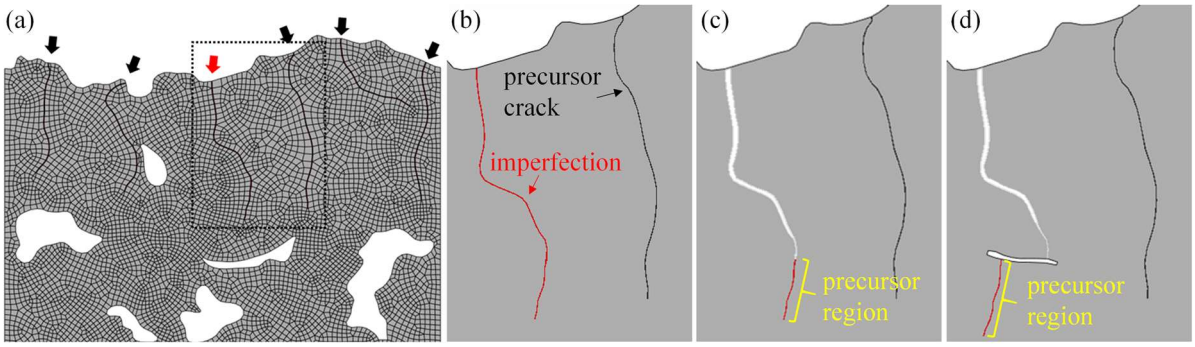

Figure 4 (a) FE mesh derived from Figure 2 (a). The arrows indicate the introduced microcracks. (b-d): magnified view of the rectangular region in (a) for the three cases investigated. The yellow braces highlight the precursor regions at the crack tips.

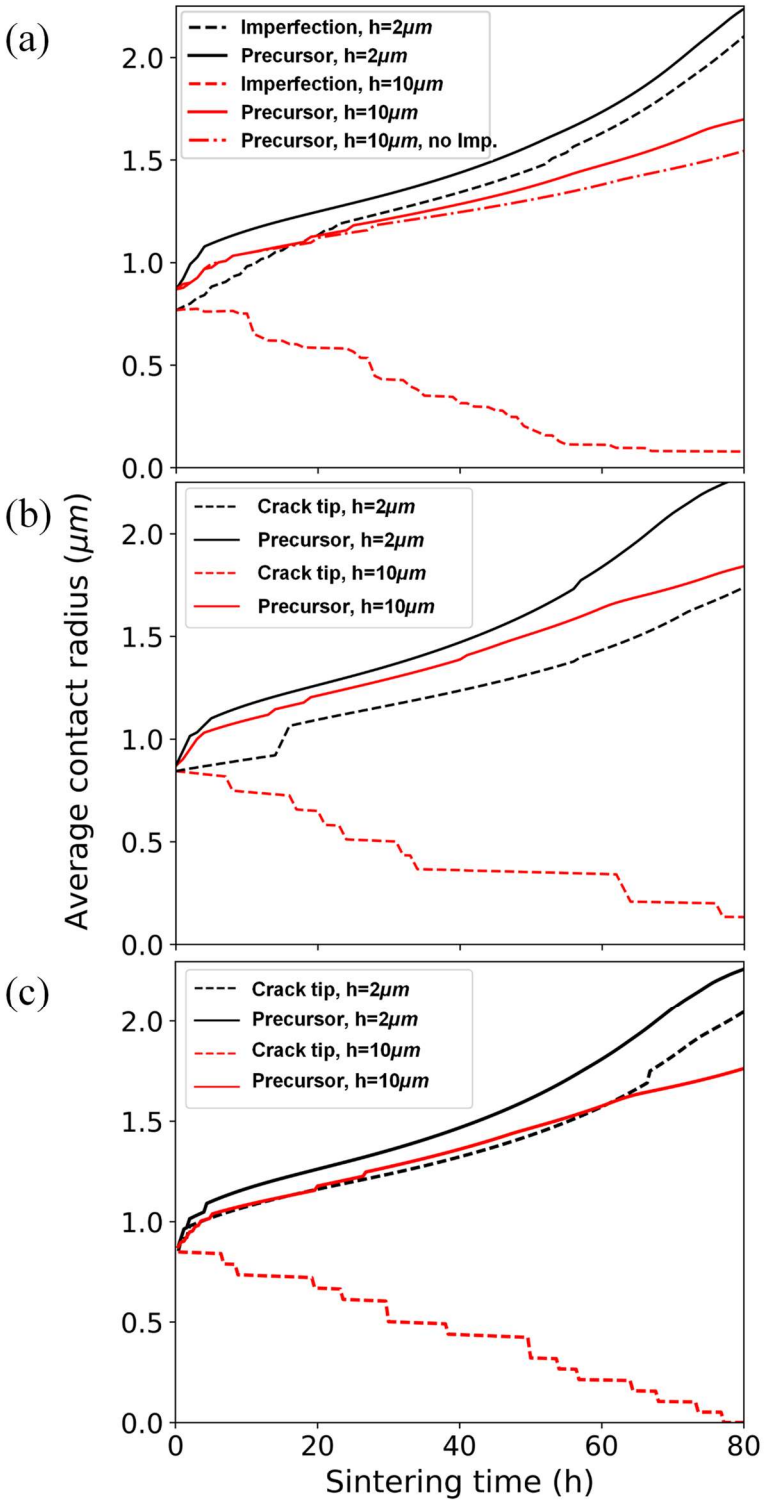

Figure 5 Temporal evolution of the predicted average asperity contact radius at (a) the imperfection; (b) and (c) the precursor region at the crack tip together with that at the neighbouring precursor crack for a YSZ splat thickness of 2μm and 10μm respectively.

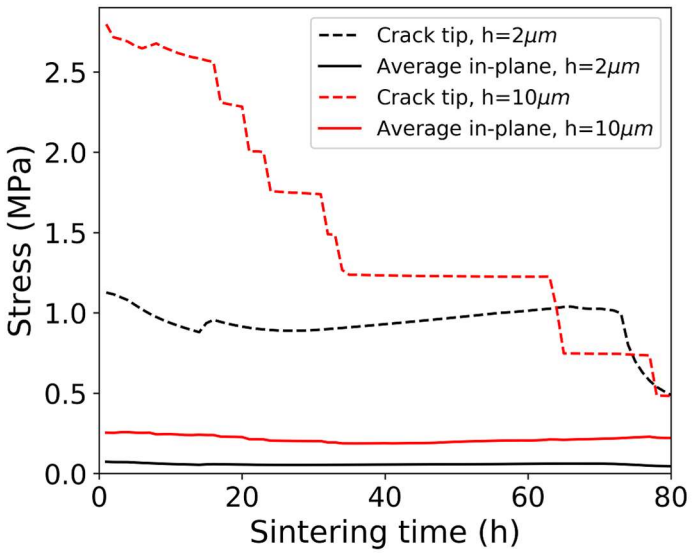

Figure 6 Evolution of the in-plane stress and surface traction averaged over the precursor region for h=2µm and 10µm respectively.

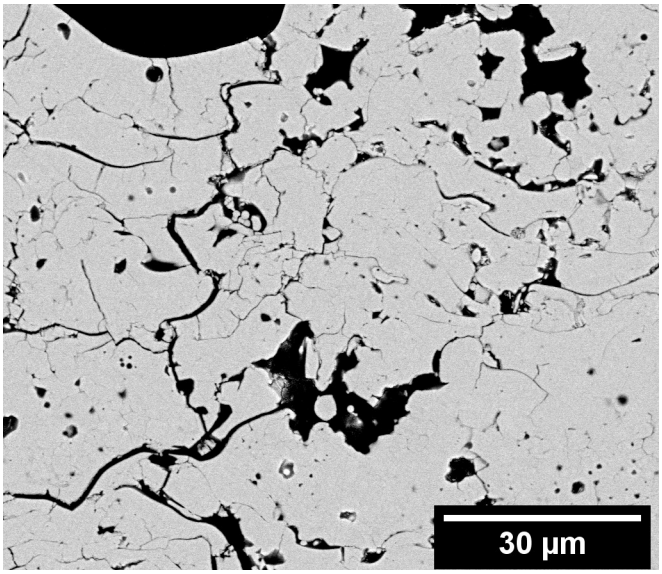

Figure 7 Cross-sectional SEM micrograph showing a sintering crack that has been deflected by the inter-splat cracks at the coating surface during constrained sintering.

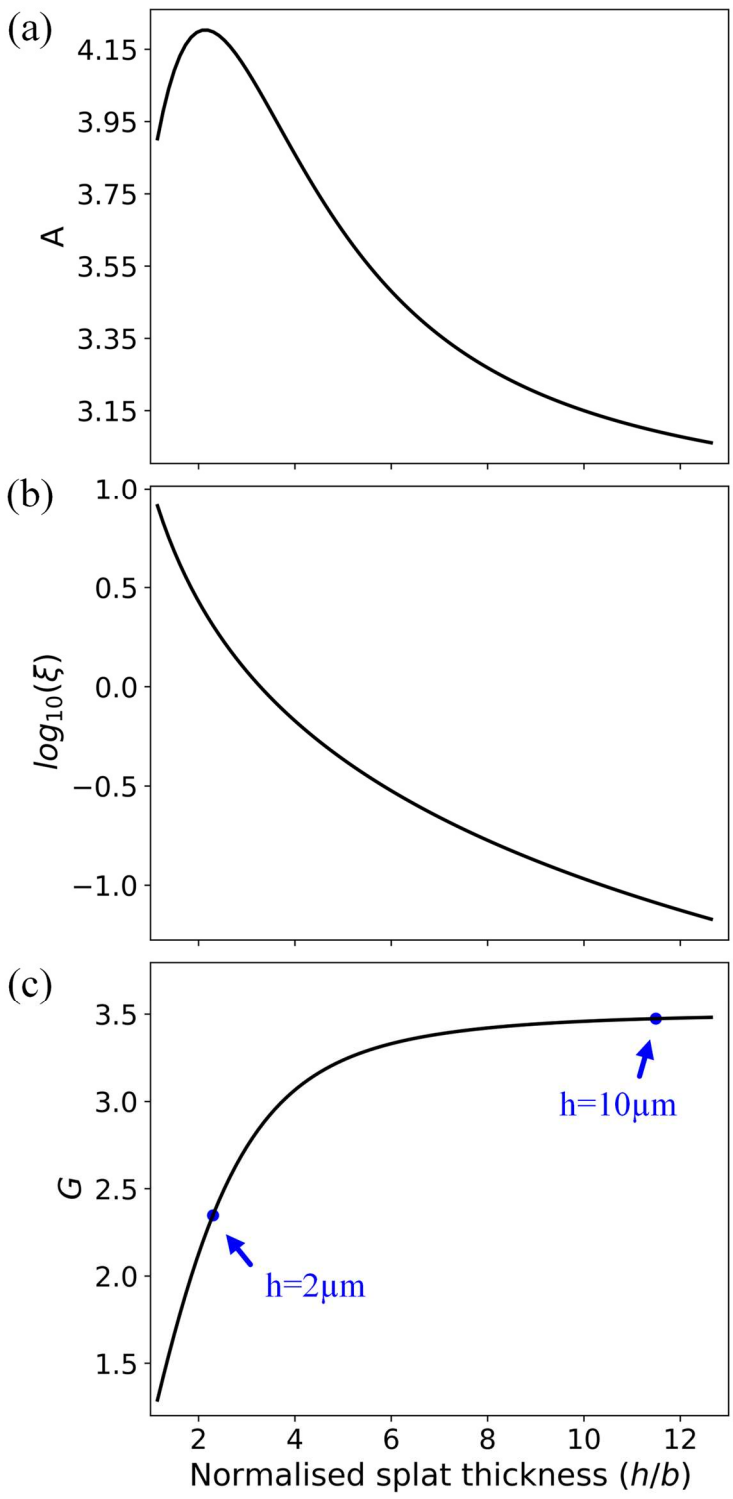

Figure 8 Plots of (a) the degree of anisotropy A in Eqn. (7); (b) the logarithm of the relative viscosity ξ in Eqn. (3) and (c) the geometric factor G in Eqn. (9) with respect to the normalised splat thickness. The splat thickness has been normalised against the asperity contact radius.

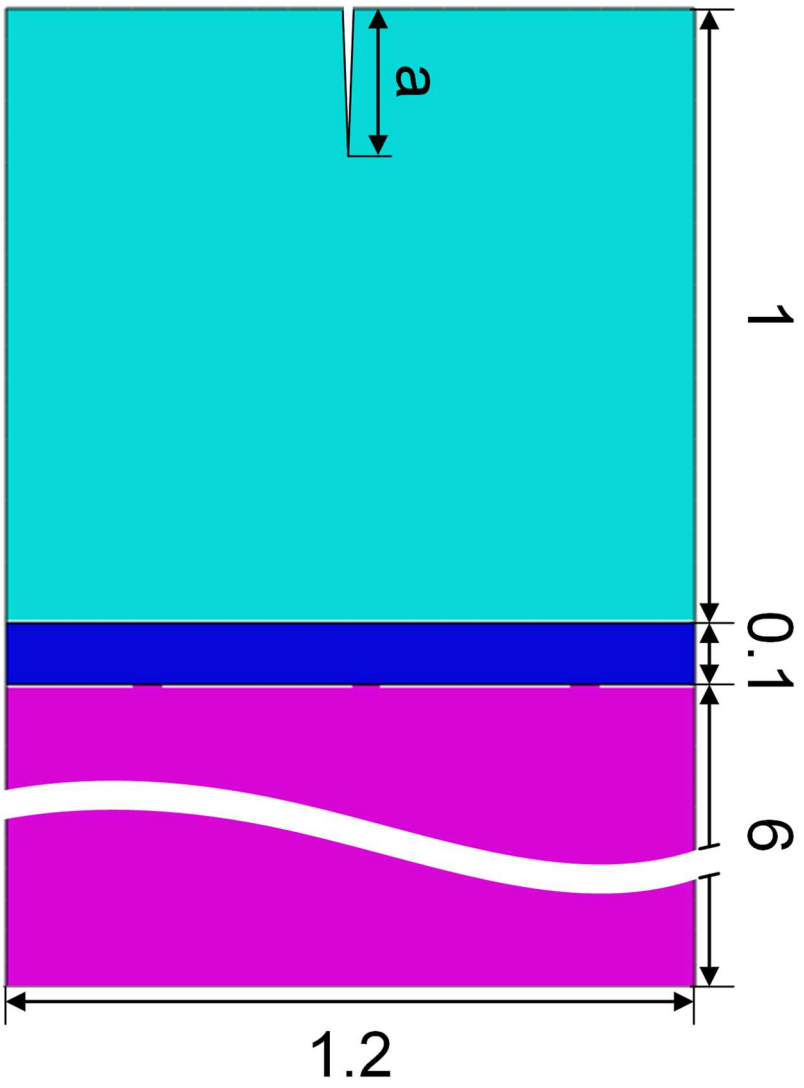

Figure 9 Schematics of the repeating unit with a crack of length a in the middle. Periodic boundary conditions are applied to both sides of the area.

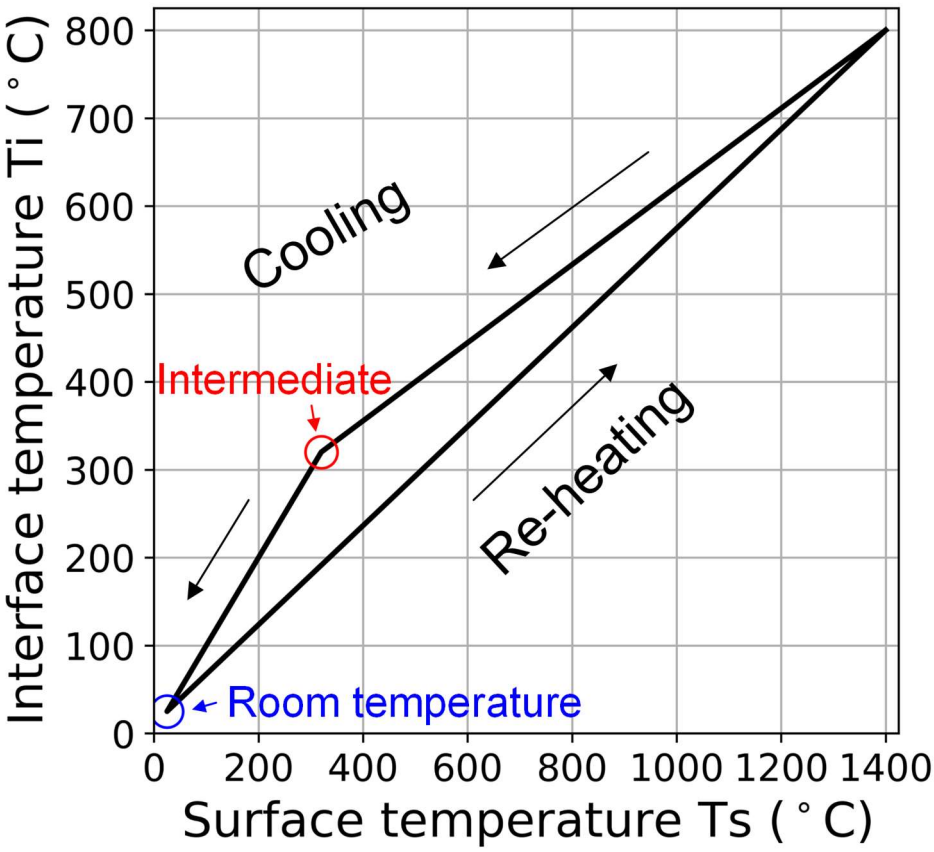

Figure 10 The cool down/reheat cycle from an initial hold temperature during the sintering test down to room temperature via an intermediate state upon cooling and reheating to the hold temperature.

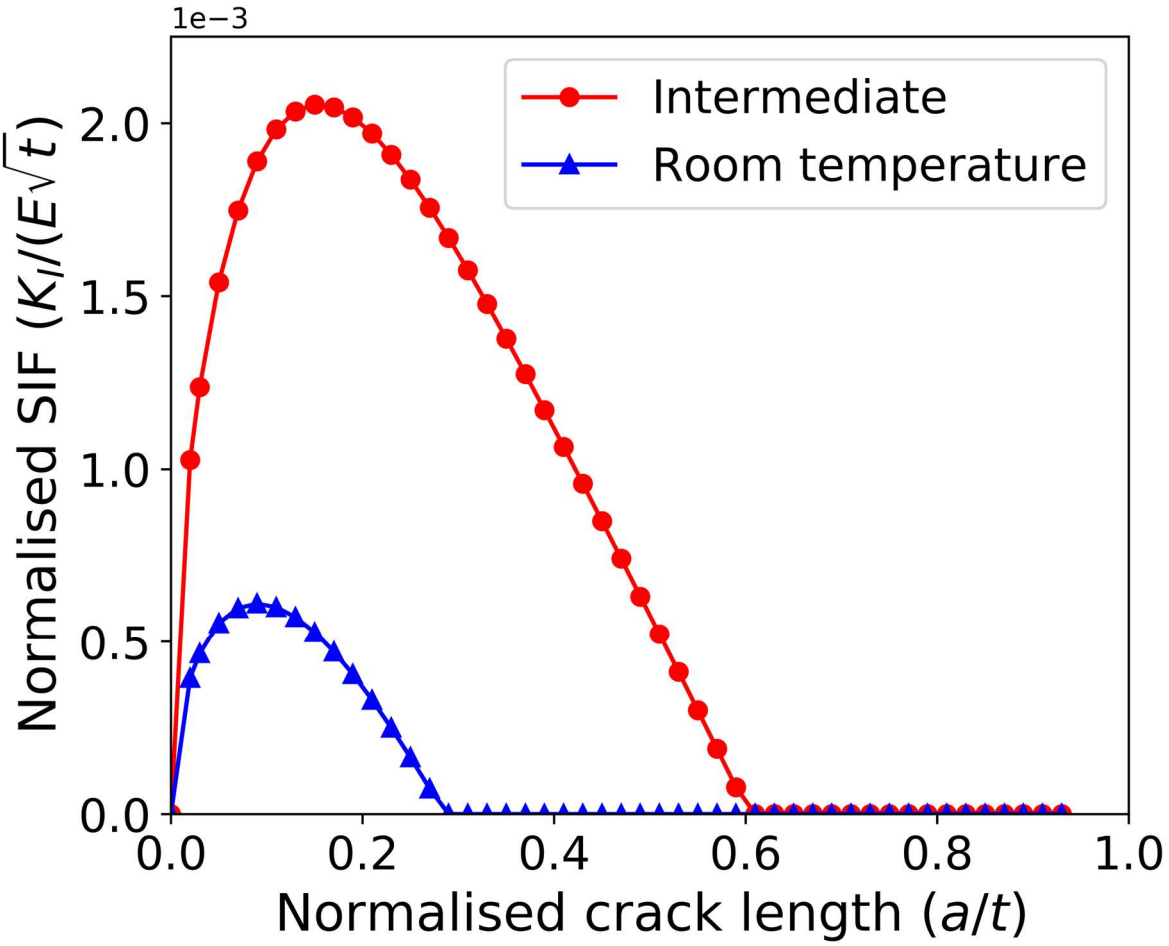

Figure 11 Variation of the stress intensity factor normalised against the coating's in-plane modulus with the initial vertical crack length normalised against the coating thickness at the intermediate temperature (red) and room temperature (blue).

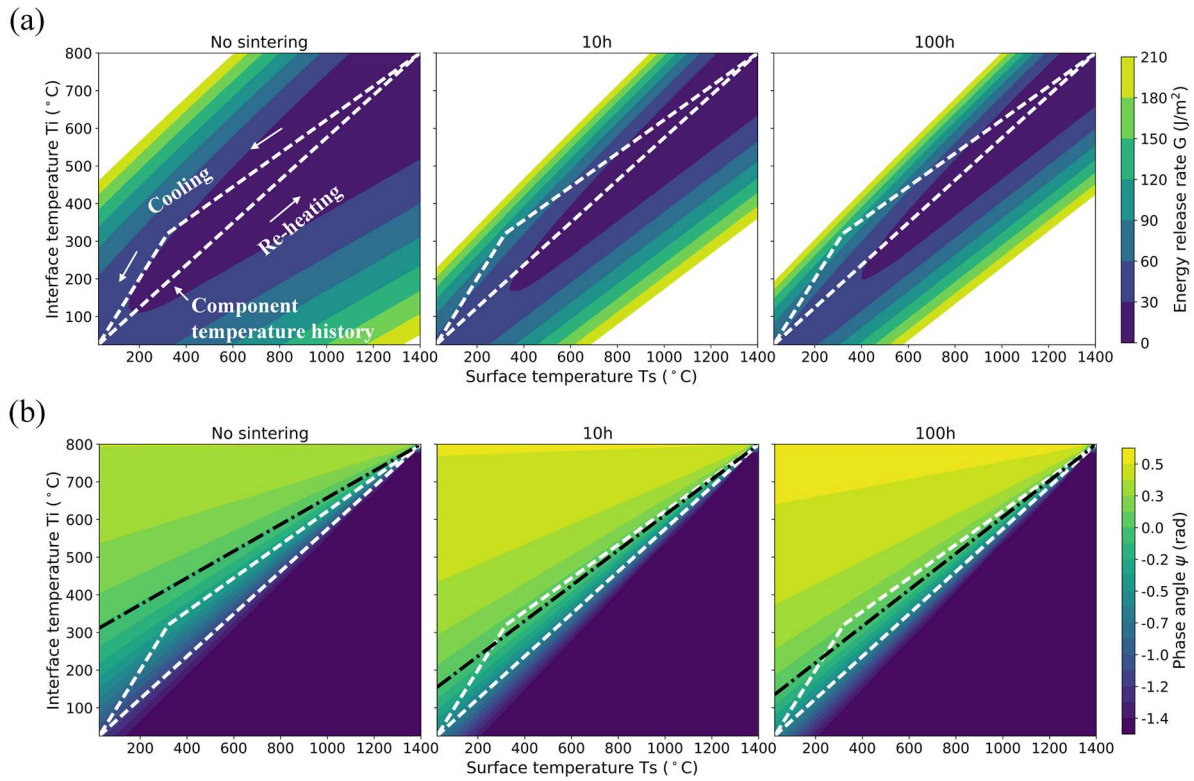

Figure 12 Contours of (a) energy release rate and (b) the mode mixity as a function of the instantaneous temperature distribution when the coating with thickness of 1mm cools down from the sintering temperature (1400°C at TBC surface and 800°C at interface) after sintering for different periods. The white lines indicate the component temperature history in one cooling-reheating cycle. The black dash lines in (b) show the instants where the SIF for a delamination crack is pure Mode I.

Supplemental Materials: Constrained sintering and cracking of air plasma sprayed thermal barrier coatings: Experimental observation and modelling

Xun Zhang[1, *], Alan C.F. Cocks[1], Yoshifumi Okajima[2], Kazuma Takeno[2], Taiji Torigoe[2]

[1]Department of Engineering Science, University of Oxford, Parks Road, Oxford OX1 3PJ, UK

[2]Mitsubishi Heavy Industries, Ltd. 1-1 Shinhama, 2-chome, Arai-cho, Takasago, Hyogo, 676-8686, Japan

1: Threshold in-plane stress for crack propagation

The threshold level of in-plane stress for crack propagation at the sintering temperature is derived here. Consider a coating containing a vertical crack of length a and subjected to an in-plane stress σ as shown in Figure S1. This in-plane stress is generated due to the constraint imposed by the substrate on the shrinkage (densification) of the porous coating. The crack length a is considered to be much smaller than the thickness of the coating.

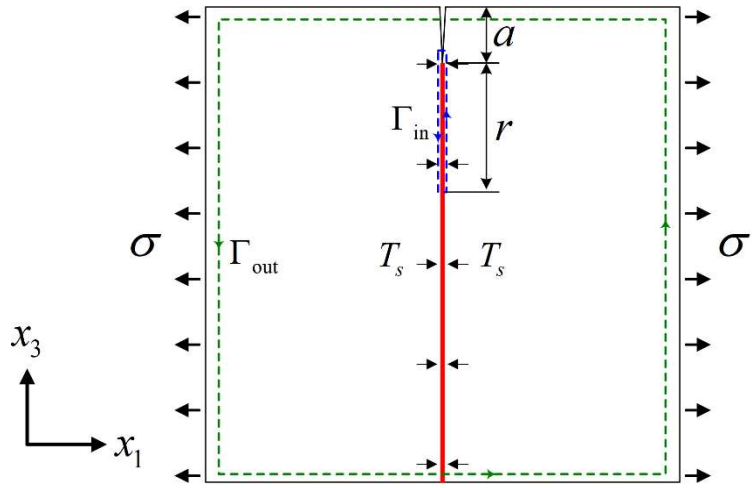

Figure S1 Schematics of the crack in a large plate with a cohesive type sintering zone running across the entire height of the plate (the red line). The plate is subject to a horizontal stress of σ. A constant traction of T_s is prescribed in the sintering zone.

The bulk material is assumed to undergo linear, transversely isotropic creep with the x_3 - direction normal to the plane of isotropy according to Eqn. 4 in the main manuscript. A cohesive type sintering zone is embedded ahead of the crack tip where a sintering traction T_s is prescribed. The sintering

zone can be thought of as two surfaces bridged by asperities and its opening rate is linear in the applied normal traction:

$$\dot{\delta} = \frac{\left(T_n - T_S\right)}{\lambda} \tag{S1.1}$$

For simplicity, we assume that T_s is constant along the sintering zone so that an analytical expression can be provided to highlight the main physics of crack propagation driven by a constrained sintering-induced in-plane stress, which allows us to identify the relative role of different material properties and geometrical parameters. FE modelling is required in order to account for the variation of T_s along the sintering zone.

The opening rate at the crack tip is derived utilising the path independence of the C^*-integral (1). The C^*-integral along the inner contour as shown in Figure S1 is evaluated as:

$$\begin{aligned} C^*_{\text{in}} &= \int W dx_1 + T_i \frac{\partial u_i}{\partial x_3} ds \\ &= \frac{\lambda}{2}\dot{\delta}_r^2 + T_s\dot{\delta}_r + \frac{\lambda}{2}\dot{\delta}_t^2 + T_s\dot{\delta}_t - \frac{\lambda}{2}\dot{\delta}_r^2 - T_s\dot{\delta}_r \\ &= \frac{\lambda}{2}\dot{\delta}_t^2 + T_s\dot{\delta}_t \end{aligned} \tag{S1.2}$$

Now consider the C^*-integral along the outer contour. In the absence of the sintering zone, the integral is given as (2):

$$\begin{aligned} C^* &= 1.12^2 \pi a \sigma^2 \sqrt{\frac{\mathrm{H}_{11}^{'}\mathrm{H}_{33}^{'}}{2}} \left[\sqrt{\frac{\mathrm{H}_{33}^{'}}{\mathrm{H}_{11}^{'}}} + \frac{\mathrm{H}_{13}^{'} + 2\mathrm{H}_{55}^{'}}{\mathrm{H}_{11}^{'}} \right]^{1/2} \\ &= 1.12^2 \pi a \sigma^2 \mathrm{H}_{11}^{'} \mathrm{A} \end{aligned} \tag{S1.3}$$

The contour intersects the sintering zone far away from the crack tip such that:

$$T_n = \sigma \tag{S1.4}$$

The contribution from the sintering zone to the integral along the outer contour is given as:

$$\int W dx_1 = \frac{\lambda}{2}\dot{\delta}^2 + T_s\dot{\delta} \tag{S1.5}$$

The opening rate at this point is:

$$\dot{\delta} = \frac{\sigma - T_s}{\lambda} \tag{S1.6}$$

Inserting Eqn. (S1.6) into Eqn. (S1.5) and adding the result to Eqn. (S1.3) gives:

$$C^*_{\text{out}} = 1.12^2\pi a\sigma^2 \mathrm{H}'_{11}\mathrm{A} + \frac{\lambda}{2}\left[\left(\frac{\sigma}{\lambda}\right)^2 - \left(\frac{T_s}{\lambda}\right)^2\right] \tag{S1.7}$$

Utilising the path independency of the creep J-integral C^* (1), the opening rate at the crack tip can be related to the far-field stress σ as:

$$\dot{\delta}_t = \frac{1}{\lambda}\left[\left(1 + 2.5\pi a\lambda \mathrm{H}'_{11}\mathrm{A}\right)^{1/2}\sigma - T_s\right] \tag{S1.8}$$

$\dot{\delta}_t > 0$ suggests that the crack opens and grows. Letting $\dot{\delta}_t = 0$ gives Eqn. (6) in the paper.

In order to validate Eqn. (6), the boundary value problem described in Figure S1 is solved by the FE method using ABAQUS 2017. The bulk material follows a viscoelastic response. The Young's modulus and Possion's ratio of bulk YSZ is used. Its creep response is given by Eqn. (4) in the paper. The constitutive response of the sintering zone is given by Eqn. (S1.1), which is implemented as a user UEL subroutine. A penalty stiffness for the interface element has been chosen so that the elastic opening component has limited effect on the FE results.

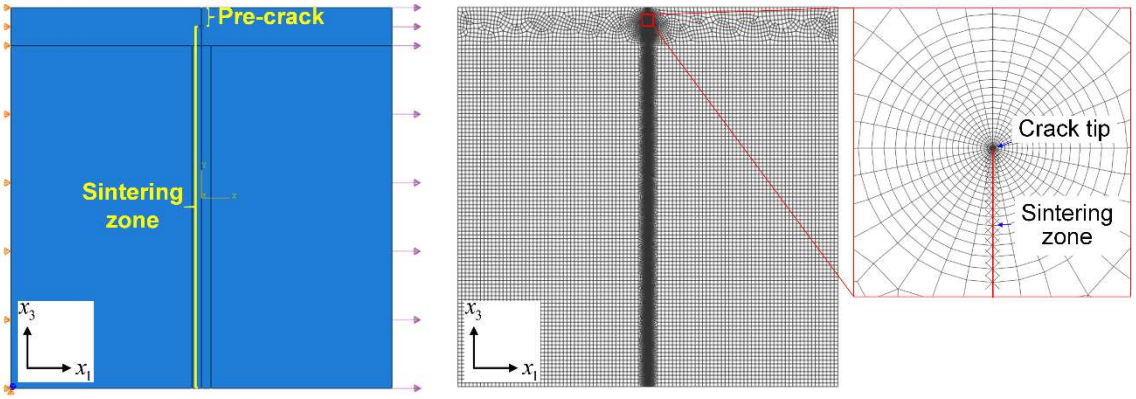

Figure S2 Geometry and FE mesh for the plate and a zoom-in view of the mesh at the crack tip. Interface element is inserted along the sintering zone as highlighted by the vertical red line.

Figure S2 shows a typical FE mesh for the geometry. The plate measures 1mm x 1mm and a pre-crack with $a = 0.05$ mm is located in the middle of the region shown. 4-node plane strain elements have been used to discretise the plate, while interface elements (UEL) have been inserted along a line directly ahead of the crack. The mesh comprises 26869 continuum elements and 956 interface elements.

A series of FE models have been run using different values for the viscosity of the sintering zone (i.e. λ in Eqn. (S1.1)) while the other material properties are kept constant. For each set of parameters, the separation rate at the crack tip is determined for a series of different applied stresses. This allows the critical stress for the crack tip to open can be determined. The obtained threshold level of in-plane stress for a crack tip to open is plotted in Figure S3 together with predictions of Eqn. (6), which serves to validate Eqn. (6).

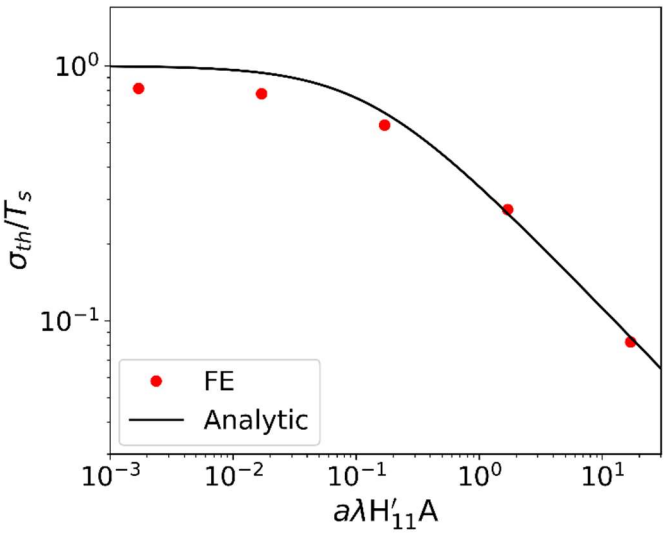

Figure S3 The threshold level of in-plane stress normalised against the sintering traction within the sintering zone determined by FE and Eqn. 6 as a function of $a\lambda \mathrm{H}_{11}^{'}\mathrm{A}$.

2: Fracture mechanics analysis for a delamination crack

The stress intensity factors, energy release rate and phase angle are given by (3, 4):

$$
\begin{aligned}
K_I &= 0.434\frac{P}{\sqrt{\hat{A}t}} + 0.558\frac{M}{\sqrt{\hat{I}t^3}} \\
K_{II} &= 0.558\frac{P}{\sqrt{\hat{A}t}} - 0.434\frac{M}{\sqrt{\hat{I}t^3}} \\
G &= \frac{(1-\nu^2)}{E(t)}(K_I^2 + K_{II}^2) \\
\psi &= \tan^{-1}\left(\frac{K_{II}}{K_I}\right)
\end{aligned}
\tag{S2.1}
$$

where $\hat{A}$ and $\hat{I}$ are dimensionless parameters arising from the variation of $E(y)$ along the coating's thickness direction and are given by (3):

$$\hat{A} = \int_0^t \frac{E(y)}{tE(t)}dy \tag{S2.2}$$

$$\hat{I} = \frac{1}{t^3}\int_0^t \frac{E(y)}{E(t)}(y-\bar{y})^2 dy \tag{S2.3}$$

where the position of the neutral axis $\bar{y}$ reads:

$$\bar{y} = \frac{1}{\hat{A}}\int_0^t \frac{yE(y)}{tE(t)}dy \tag{S2.4}$$

P and M are the equivalent end load and bending moment (per unit thickness) acting through and about the neutral axis of the equivalent section respectively (3):

$$P = \int_0^t \sigma(y)dy \tag{S2.5}$$

$$M = \int_0^t \sigma(y)(y-\bar{y})dy \tag{S2.6}$$

Notice from Eqn. (10) that $\sigma(y)$ scales with the coating's in-plane modulus $E(y)$.

Upon combining Eqn. (S2.1)-(S2.6), the energy release rate and mode mixity can be determined as a function of the instantaneous temperature distribution as characterised by the temperature at the coating surface and interface with a linear variation in between.

References

1. Elmukashfi E, Cocks ACF. A theoretical and computational framework for studying creep crack growth. Int J Fracture. 2017;208(1-2):145-70.
2. Sih GC, Paris PC, Irwin GR. On Cracks in Rectilinearly Anisotropic Bodies. Int J Fract Mech. 1965;1(3):189-203.
3. Fleck NA, Cocks ACF, Lampenscherf S. Thermal shock resistance of air plasma sprayed thermal barrier coatings. J Eur Ceram Soc. 2014;34(11):2687-94.
4. Suo Z, Hutchinson JW. Steady-State Cracking in Brittle Substrates beneath Adherent Films. Int J Solids Struct. 1989;25(11):1337-53.